Lawrence Berkeley National Laboratory
Materials Sciences

Title
Composition-dependent ordering transformations in Pt–Fe nanoalloys

Permalink
https://escholarship.org/uc/item/027064sf

Journal
Proceedings of the National Academy of Sciences of the United States of America, 119(14)

ISSN
0027-8424

Authors
Chen, Xiaobo
Zhang, Siming
Li, Can
et al.

Publication Date
2022-04-05

DOI
10.1073/pnas.2117899119

Peer reviewed

Composition-dependent ordering transformations in Pt–Fe nanoalloys

Xiaobo Chen[a,b], Siming Zhang[c], Can Li[d], Zhijuan Liu[e], Xianhu Sun[a,b], Shaobo Cheng[f,g], Dmitri N. Zakharov[e], Sooyeon Hwang[e], Yimei Zhu[f], Jiye Fang[d], Guofeng Wang[c], and Guangwen Zhou[a,b,1]

Despite the well-known tendency for many alloys to undergo ordering transformations, the microscopic mechanism of ordering and its dependence on alloy composition remains largely unknown. Using the example of $Pt_{85}Fe_{15}$ and $Pt_{65}Fe_{35}$ alloy nanoparticles (NPs), herein we demonstrate the composition-dependent ordering processes on the single-particle level, where the nanoscale size effect allows for close interplay between surface and bulk in controlling the phase evolution. Using in situ electron microscopy observations, we show that the ordering transformation in $Pt_{85}Fe_{15}$ NPs during vacuum annealing occurs via the surface nucleation and growth of $L1_2$-ordered Pt_3Fe domains that propagate into the bulk, followed by the self-sacrifice transformation of the surface region of the $L1_2$ Pt_3Fe into a Pt skin. By contrast, the ordering in $Pt_{65}Fe_{35}$ NPs proceeds via an interface mechanism by which the rapid formation of an $L1_0$ PtFe skin occurs on the NPs and the transformation boundary moves inward along with outward Pt diffusion. Although both the "nucleation and growth" and the "interface" mechanisms result in a core–shell configuration with a thin Pt-rich skin, $Pt_{85}Fe_{15}$ NPs have an $L1_2$ Pt_3Fe core, whereas $Pt_{65}Fe_{35}$ NPs are composed of an $L1_0$ PtFe core. Using atomistic modeling, we identify the composition-dependent vacancy-assisted counterdiffusion of Pt and Fe atoms between the surface and core regions in controlling the ordering transformation pathway. This vacancy-assisted diffusion is further demonstrated by oxygen annealing, for which the selective oxidation of Fe results in a large number of Fe vacancies and thereby greatly accelerates the transformation kinetics.

Pt–Fe nanoparticles | alloy composition | in situ electron microscopy | chemical ordering

Many alloys tend to undergo ordering transformations from a random solid solution all the way to fully ordered ground-state intermetallics. The driving force of such an ordering process is the chemical attraction between like and unlike atoms, that is, the occupation of neighboring lattice sites by a different type of atoms is energetically more favorable than that by the same type of atoms (1). Despite this well-recognized pairwise interaction in driving the ordering transformation (2), dynamically understanding the microscopic processes governing the onset, promotion, and termination of an ordering transformation has rarely been attained, mainly due to the lack of suitable tools capable of spatially and temporally tracking the ordering processes including atom mobility, nucleation and growth of ordered domains and the resultant interface dynamics, and possible formation and structural evolution of metastable, intermediate phases. The situation becomes even more challenging for nanoscale alloys, where the significantly increased surface-area-to-volume ratio not only opens up a variety of additional freedoms to initiate an ordering transformation but also allows for kinetic interplay between the surface and bulk due to their close proximity (3, 4). Deconvoluting such surface–bulk interplay is not achievable with ensemble structure analyses such as powder X-ray diffraction (PXRD) that have been widely used to study the ordering processes on the global scale (5). By contrast, transmission electron microscopy (TEM) is capable of providing local structural and chemical information to a level of spatial resolution that is unapproachable by most other techniques (6, 7). The in situ heating TEM holder can be used to study the structural and compositional evolution of solid materials during heat treatment, either in a vacuum or under a gas environment. Such an in situ capability is particularly useful to monitor the ordering transformation dynamics on the single-nanoparticle (NP) level (3, 6, 8).

In this study we demonstrate, using in situ TEM, the microscopic processes controlling the ordering transformation through the surface–bulk interplay in Pt–Fe NPs and new features rendered by variations in alloy composition and chemical stimuli. Our rationale for choosing Pt–Fe NPs as the model system is twofold. First, although Pt–M (M = Fe, Ti, Cu, Co, etc.) bulk alloys are well known to show a strong ordering

Significance

Dynamically understanding the microscopic processes governing ordering transformations has rarely been attained. The situation becomes even more challenging for nanoscale alloys, where the significantly increased surface-area-to-volume ratio not only opens up a variety of additional freedoms to initiate an ordering transformation but also allows for kinetic interplay between the surface and bulk due to their close proximity. We provide direct evidence of the microscopic processes controlling the ordering transformation through the surface–bulk interplay in Pt–Fe nanoalloys and new features rendered by variations in alloy composition and chemical stimuli. These results provide a mechanistic detail of ordering transformation phenomena which are widely relevant to nanoalloys as chemical ordering occurs in most multicomponent materials under suitable environmental bias.

tendency (9, 10), nanostructuring of the alloys not only drives the thermodynamic state far away from the bulk phase but also results in shorter transport pathways, faster diffusion, and more rapid transformation kinetics with respect to their bulk counterparts (11). Second, Pt-based alloy NPs are widely used as cathode electrocatalysts for oxygen reduction reaction (12–15) and anode electrocatalysts for oxygen evolution reaction (16), and structurally ordered intermetallic NPs display superior electrocatalytic activity and durability along with decreased Pt loading compared with Pt/C in electrochemical reactions (17–19). However, as-synthesized Pt-based alloy NPs typically form as random solid solutions that suffer from rapid composition and structure degradation during electrocatalytic processes due to the oxidation and dissolution of the alloy components (17). Therefore, posttreatment processing such as high-temperature annealing has long been employed to transform the random solid solution into an ordered intermetallic phase that has improved electroactivity and durability arising from the stronger Pt–M heteroatomic bonding and a more negative enthalpy of formation compared to its disordered state (18). The ordering can change the electron density of states and alter the position of d-band with respect to the Fermi level, where the position of d-band depends on long-range order of the ordered phase (19–22). Therefore, understanding the ordering transformations in these alloy NPs forms the basis for improving the catalytic efficiency and durability. Our current understanding of the ordering processes in such alloy NP catalysts is largely derived from "quench-and-look" studies, where the catalysts are quenched after a certain amount of annealing time, followed by ex situ characterization of the postannealed NPs (23, 24). However, short-lived intermediate states are difficult to capture with this approach and the ordering mechanism may be more complex than that expected from straightforward postmortem studies. Another issue for postexamination is atmospheric contamination that may bring controversies in understanding the reaction mechanism (25–27). To overcome these shortcomings, in situ tools, including PXRD and TEM, have been used to study the ordering processes during thermal annealing (3–6). By monitoring the relative intensity evolution of the superlattice peaks, PXRD is capable of providing important information on the degree of ordering for an assemble of Pt alloy NPs. In situ TEM can complement the PXRD by providing dynamic information on the atomic structure and morphological evolution of individual NPs upon the heating. However, to the best of our knowledge, none of the studies have attempted to address the ordering transformation mechanism and correlate it with the alloy composition and the annealing atmosphere.

Herein, we report the real-time, atomic-scale TEM observations of the ordering transformations in Pt–Fe NPs during high-temperature annealing. Two distinct alloy compositions, i.e., $Pt_{85}Fe_{15}$ and $Pt_{65}Fe_{35}$, which deviate from the ideal stoichiometry of intermetallic compounds, are chosen to study the ordering mechanism and its dependence on the alloy composition of the NPs. We have performed a comparative study by annealing under vacuum and O_2 gas environments, where the former yields the intrinsic ordering behavior for pristine NPs whereas the latter has practical relevance because of the intentional or unavoidable presence of oxidative gas species (O_2, H_2O, etc.) in the annealing atmosphere for a typical heat-treatment process. By combining with atomistic modeling, this mechanistic study provides microscopic mechanism underlying the onset and progression of the ordering transformation from the surface to the bulk of the NPs and the phase transformation pathways associated with the alloy composition and annealing

atmosphere. As compared to pure metal NPs, the complexity is increased manifold for multicomponent NPs, the microscopic insights obtained from the in situ TEM observations open vistas of new opportunities for a synergistic realization of composition and phase via tuning the chemical ordering process through its intrinsic and extrinsic interdependence on the alloy composition and annealing atmosphere.

Results

Pt–Fe alloy NPs were synthesized through a wet chemistry approach (28) (see *Materials and Methods* and *SI Appendix,* Figs. S1–S4). Fig. 1*A* illustrates a representative high-angle annular dark-field (HAADF) image of the as-synthesized $Pt_{85}Fe_{15}$ NPs, showing the nearly square or rectangular shapes with an average size of ∼10 nm. Fig. 1*B* illustrates an atomically-resolved HAADF-STEM (scanning TEM) image of a typical $Pt_{85}Fe_{15}$ NP along the [100] zone axis, where the uniform image contrast of the atomic columns confirms the single-phase, random solid solution. Fig. 1*C* corresponds to a high-resolution TEM (HRTEM) image of a $Pt_{85}Fe_{15}$ NP along the [100] zone axis, where the uniform lattice contrast and the absence of superlattice diffraction spots in the diffractogram (Fig. 1*C, Inset*) further evidence the random solid solution nature with a face-centered cubic (*fcc*) lattice structure. The diffraction spots in the diffractogram correspond to the (200) reflections and the d-spacing is determined to be ∼1.95 Å. Fig. 1*D* shows the STEM-EDS (energy-dispersive X-ray spectroscopy) line scan across a $Pt_{85}Fe_{15}$ NP showing the relatively uniform alloy composition without obvious surface segregation of the alloying elements.

Fig. 1 *E–G* correspond to the HAADF and HRTEM characterization of the as-synthesized $Pt_{65}Fe_{35}$ NPs, showing features (shape, size, and random solid-solution) similar to $Pt_{85}Fe_{15}$ NPs. The {200} interplanar spacing measured from the HRTEM image of $Pt_{65}Fe_{35}$ NPs is ∼1.94 Å, slightly smaller than the corresponding value of the {200} planes of $Pt_{85}Fe_{15}$ NPs. This composition-dependent lattice spacing is further confirmed by synchrotron X-ray diffraction measurements (*SI Appendix,* Fig. S2 and Table S2), showing that the $Pt_{65}Fe_{35}$ sample has a slightly smaller d-spacing than that of $Pt_{85}Fe_{15}$ sample, consistent with Vegard's law (29, 30). Fig. 1*F, Inset* is an enlarged view of the surface region of the $Pt_{65}Fe_{35}$ NP, showing that both the surface region and the bulk display the same *fcc* lattice of the random solid solution. However, the atomic columns in the outermost two to three atomic layers show much weaker HAADF image intensity than that in the deeper region, which indicates the enrichment of Fe in the surface region, as confirmed by EDS linescan (Fig. 1*H*) and mapping (*SI Appendix,* Figs. S3 and S4).

In situ vacuum annealing is performed inside a STEM using a microelectrochemical system (MEMS)-based heating holder. Fig. 2 presents in situ HAADF-STEM images of the ordering-induced atomic structure evolution in a $Pt_{85}Fe_{15}$ NP, viewed along the [100] zone axis. To avoid any possible effect from the long electron exposure on the ordering process, the beam is on only when acquiring STEM images. As shown in Fig. 2*A*, the square-shaped NP initially has a solid solution structure with randomly distributed Fe and Pt atoms. After a time elapse of 1 min, nucleation of $L1_2$-Pt_3Fe domains occurs around the surface, as marked by the dashed black lines in Fig. 2*B*, where the $L1_2$ ordering is evidenced by the characteristic arrangement of bright (Pt) and bright/dim (Pt/Fe) atom columns alternate on the {100} planes (more detail in *SI Appendix,* Fig. S5). The
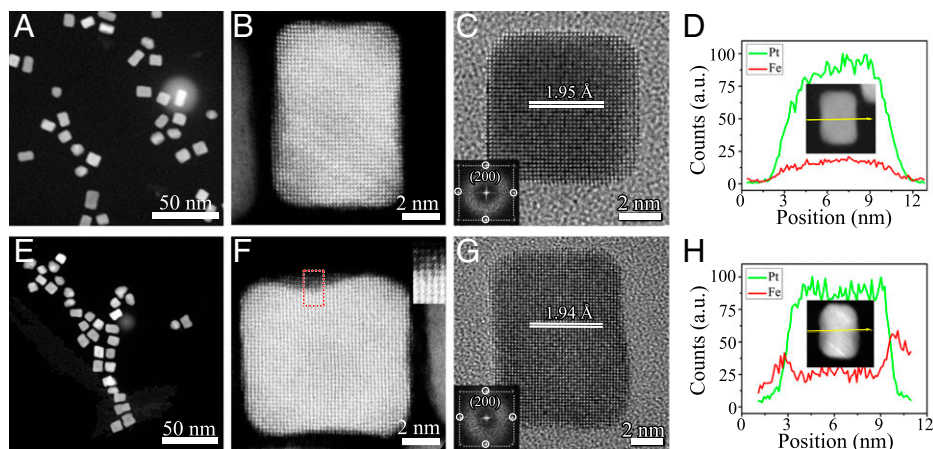
Fig. 1. TEM characterization of as-synthesized Pt–Fe NPs. (*A*) Low-magnification HAADF-STEM image of $Pt_{85}Fe_{15}$ NPs. (*B* and *C*) Atomically resolved HAADF and HRTEM images of $Pt_{85}Fe_{15}$ NPs along the [100] axis. (*C*, *Inset*) A diffractogram of the HRTEM image. (*D*) STEM-EDS line scan across a $Pt_{85}Fe_{15}$ NP along the yellow arrow. (*E*) Low-magnification HAADF-STEM image of $Pt_{65}Fe_{35}$ NPs. (*F* and *G*) Atomically resolved HAADF-STEM and HRTEM images of $Pt_{65}Fe_{35}$ NPs along the [100] zone axis. (*F*, *Inset*) An enlarged HAADF view of the surface region marked by the red dashed rectangle, revealing significantly weakened image intensity of the outermost two to three atomic layers. (*G*, *Inset*) A diffractogram of the HRTEM image. (*H*) STEM-EDS line scan across a $Pt_{65}Fe_{35}$ NP along the yellow arrow, showing the surface segregation of Fe.

nucleation, growth, and coalescence of $L1_2$ Pt_3Fe domains propagate into the bulk (Fig. 2 *C* and *D*) and eventually transform the NP into a core–shell structure consisting of a thin Pt shell and the $L1_2$ Pt_3Fe core (Fig. 2 *E* and *F*). The existence of the Pt shell is confirmed by EDS maps of the well-annealed NP, showing a larger NP in the Pt map (Fig. 2*G*) than that in the Fe map (Fig. 2*H*) and the stronger Pt signal of the outer region in the combined Pt/Fe map (Fig. 2*I*). The formation of a similar Pt_3Fe/Pt core–shell structure is confirmed by examining a large number of well-annealed $Pt_{85}Fe_{15}$ NPs (*SI Appendix*, Fig. S6).

Surprisingly, our in situ STEM imaging reveals that the formation of the Pt shell occurs via decomposing the initially formed $L1_2$ Pt_3Fe domains around the surface during the ordering in the bulk of the NP. This is revealed by the gradual transformation of bright/dim superlattice feature in the surface region (Fig. 2 *B* and *C*) into the uniform lattice contrast upon the progressive ordering in the bulk (Fig. 2 *E* and *F*). This surface nucleation and growth process of $L1_2$ Pt_3Fe domains along with the subsequent decomposition of the formed Pt_3Fe phase at the surface into the Pt skin provides important clues to the diffusion process for controlling the ordering transformation. For the composition of $Pt_{85}Fe_{15}$ NPs, the Pt_3Fe ($L1_2$) ordering requires either the rejection of excess Pt atoms and/or incorporation of additional Fe atoms. The surface region of the NPs has larger atom mobility and is thus kinetically preferred for nucleation and growth of ordered domains by rejecting excess Pt atoms to the outermost surface region along with the outward diffusion of Fe atoms from the bulk to the surface region. As marked by the dashed cyan lines in Fig. 2 *A–C*, the initially flat surface facet of the NP transforms into a curved shape with the formation and lateral growth of a small protrusion, which can be caused by the surface aggregation of the rejected Pt atoms into a Pt island. The time-sequence HAADF images in Fig. 2 *E* and *F* further demonstrate that the islanding of the excess Pt atoms also occurs on the planar surface in the projection view, where the region marked by the red dashed circle shows brighter image contrast and grows larger due to the ordering transformation induced rejection of excess Pt atoms from the bulk to the surface. This is also confirmed by the corresponding EDS mapping, where the region marked by the red dashed circle in the combined Pt and Fe map (Fig. 2*I*) shows

stronger Pt intensity and corresponds to the surface island of Pt atoms.

In addition to the surface rejection of Pt atoms and outward diffusion of Fe atoms from the bulk for the initial stage of the ordering transformation in the surface and subsurface region, our in situ STEM imaging demonstrates that the later-stage ordering transformation in the bulk of the NP involves the inward diffusion of Fe atoms from the surface region into the bulk. As shown in Fig. 2 *C–F*, the formation of the Pt skin occurs via the progressive transformation of the surface region of the initially formed $L1_2$ Pt_3Fe into pure Pt. This is due to the counterdiffusion of Fe and Pt atoms, by which the Fe atoms in the surface layer of the Pt_3Fe $L1_2$ region diffuse inward and the resulting Fe vacant sites are filled by the outward-diffusing Pt atoms from the bulk. The counterdiffusion of Pt and Fe atoms is driven by the composition disparity between the composition $Pt_{85}Fe_{15}$ in the untransformed bulk region of the NP and the ideal stoichiometry of Pt_3Fe intermetallic compound, where the outward diffusion of excess Pt atoms in the bulk in conjunction with the concurrent inward diffusion of Fe atoms from the surface is required to reach the stoichiometry for the formation of $L1_2$ Pt_3Fe in the core region. This self-sacrifice transformation of the $L1_2$ Pt_3Fe in the surface region into a Pt skin marked by the white dashed circle in Fig. 2 *E* and *F* is also favored thermodynamically due to the lower surface energy of Pt than that of $L1_2$ Pt_3Fe (31–33).

Fig. 2*J* schematically illustrates the ordering transformation process in $Pt_{85}Fe_{15}$ NPs. The ordering starts with the nucleation and growth of $L1_2$ Pt_3Fe domains in the surface region (Fig. 2 *J, i*). The growth of the ordered domains leads to their coalescence and propagation from the surface region into the bulk (Fig. 2 *J, ii*). The Pt_3Fe $L1_2$ ordering in the bulk results in outward diffusion of excess Pt atoms from the core region in conjunction with the concurrent inward diffusion of Fe atoms from the surface region, thereby transforming the surface region of the Pt_3Fe $L1_2$ phase into a pure Pt skin (Fig. 2 *J, iii*). The ordering transformation via the counterdiffusion of Pt and Fe atoms results in a core–shell structure consisting of a thin shell of Pt and a Pt_3Fe $L1_2$ ordered core (Fig. 2 *J, iv*).

Fig. 3 presents in situ HAADF-STEM image snapshots of the ordering transformation in a $Pt_{65}Fe_{35}$ NP at 700 °C in vacuum. The as-prepared NPs are of the *fcc* random solid solution of Fe-Pt, as shown in Fig. 1 and *SI Appendix*, Fig. S7. Fig. 3*A* shows an
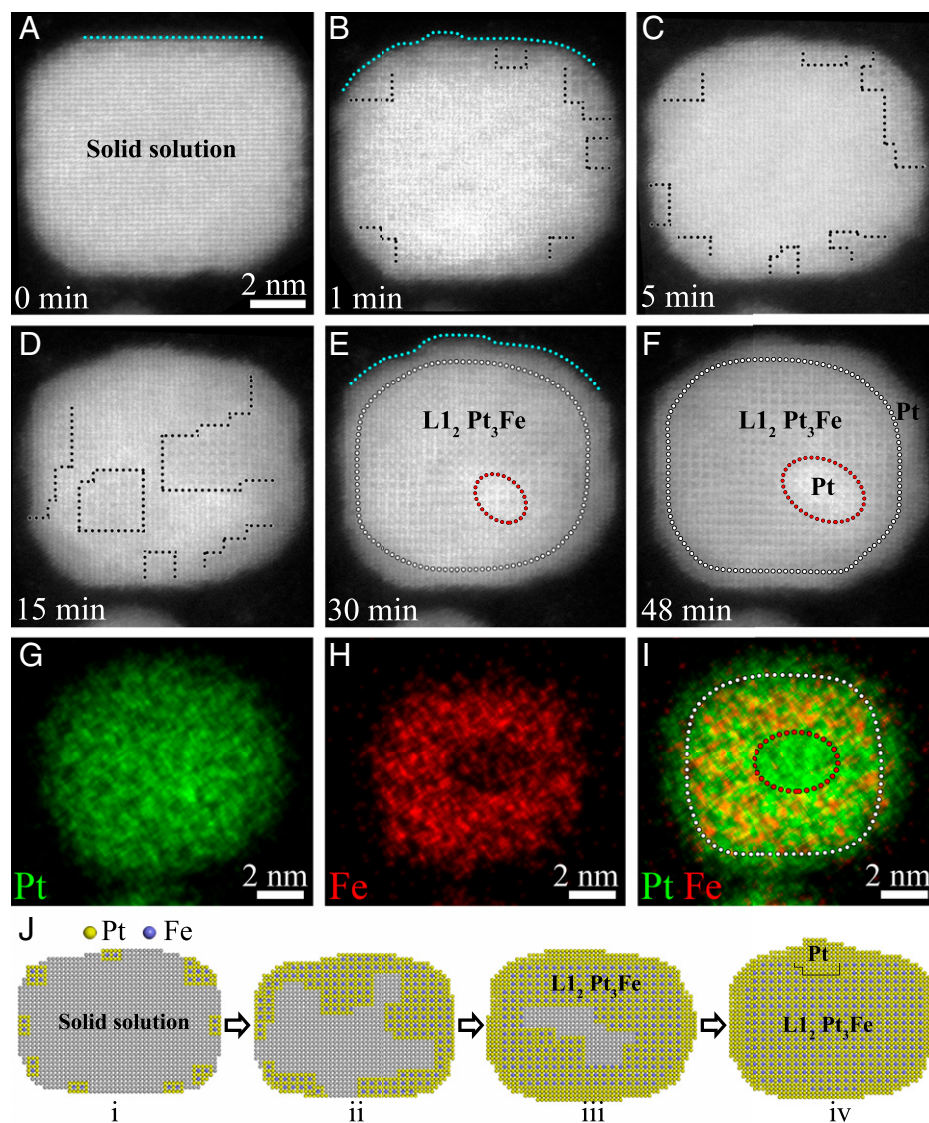
Fig. 2. In situ STEM imaging of the ordering transformation in a $Pt_{85}Fe_{15}$ NP at 700 °C and in vacuum. (*A–F*) Time-sequence HAADF image snapshots showing the surface nucleation and growth of Pt_3Fe $L1_2$ ordered domains (as marked by black dashed lines) that propagate into the bulk. The cyan lines in *A*, *B*, and *E* mark the formation of a Pt island via aggregation of Pt atoms rejected from the bulk. The white dashed circles in *E* and *F* mark the boundary between the Pt shell and the Pt_3Fe $L1_2$ ordered core. The red dashed circles in *E* and *F* indicate the region showing the brighter image contrast due to the presence of a Pt island on the planar surface. (*G* and *H*) STEM EDS maps of Pt (green) and Fe (red) and (*I*) overlay of the of the Pt and Fe EDS maps of the well-annealed NP in *F*. (*J*) Schematic illustrating the nucleation and growth mechanism of the ordering transformation in $Pt_{85}Fe_{15}$ NPs.

HAADF image of the NP, captured right after the temperature reaches 700 °C, showing that the entire surface of the NP is already covered with a continuous skin of the ordered intermetallic compound. The intermetallic skin comprises two atomic layers bright (Pt) atom columns in the outermost layer and dim (Fe) atom columns in the second layer, which match the arrangement of Pt and Fe atoms in the {001} planes of $L1_0$ PtFe (more detail in *SI Appendix,* Figs. S7 and S8). The presence of the outmost atomic layer of Pt is also confirmed by the intensity profiles taken across the HAADF image (*SI Appendix,* Fig. S7) by exploiting the atomic sensitivity of the Z contrast in the HAADF-STEM imaging. As marked by the white dashed lines in Fig. 3 *B* and *C*, the transformation boundary between the $L1_0$ PtFe skin and the random solid solution advances inward, which results in $L1_2$ ordering (Pt_3Fe) from the subsurface to the bulk. Meanwhile, the initially formed $L1_0$ PtFe skin gradually transforms to $L1_2$ Pt_3Fe (Fig. 3*C*). As a result, the entire NP is dominated by the lattice feature of $L1_2$ Pt_3Fe (Fig. 3*D*). Upon the continued annealing, however, the center region of the NP as marked by the red dashed circle in Fig. 3*E*

further transforms into a different ordered structure in which the arrangement of Pt and Fe atoms as well as the interplanar spacings match well with $L1_0$ PtFe (detail in *SI Appendix,* Fig. S8). As marked by the red dashed circle in Fig. 3*F*, the PtFe domain grows outward by consuming the surrounding Pt_3Fe. Meanwhile, the superlattice feature of the $L1_2$ Pt_3Fe is gradually lost in some of the surface and subsurface region (as marked by the purple dashed lines in Fig. 3 *E* and *F*), indicating the self-sacrifice transformation of the outer region of the $L1_2$ Pt_3Fe into a Pt skin in conjunction with the $Pt_3Fe \rightarrow$ PtFe transformation in the bulk and suggesting the tendency to form a PtFe/Pt core–shell structure upon the transformation pathway (more details in *SI Appendix,* Figs. S8 and S9). This is demonstrated in Fig. 3*G*, showing the formation of the core–shell structure for a well-annealed $Pt_{65}Fe_{35}$ NP that consists of a 1-nm-thick Pt shell and the $L1_0$ PtFe core. As shown in Fig. 3 *H–J*, the core shell structure is also compositionally confirmed by the corresponding STEM-EDS mapping of the NP. The core/shell boundary position is roughly marked with the white dashed circle in the combined Pt/Fe map (Fig. 3*J*) and the shell region shows a
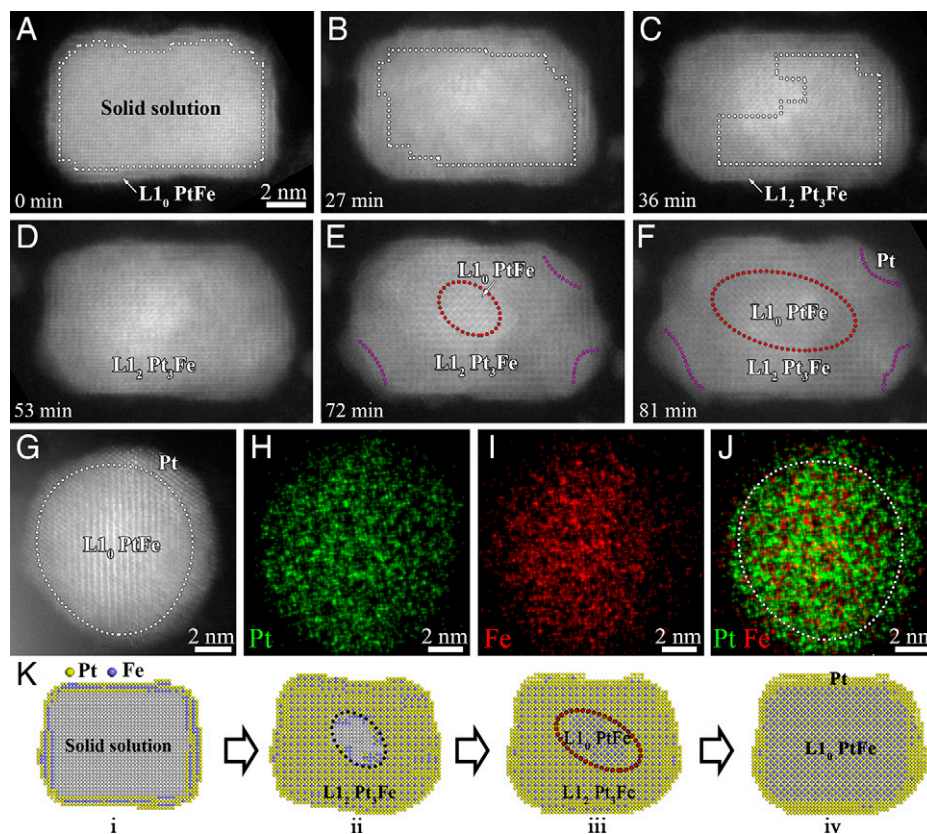
Fig. 3. In situ STEM-HAADF imaging of the ordering transformation in a $Pt_{65}Fe_{35}$ NP at 700 °C and in vacuum. (*A–F*) Time-sequenced HAADF images displaying the ordering transformation via the rapid formation of a $L1_0$PtFe shell that subsequently transform to $L1_2$ Pt_3Fe. The continued inward growth of the $L1_2$ ordered Pt_3Fe shell results in the nucleation of a $L1_0$ PtFe domain in the core region that grows outward by consuming the surrounding Pt_3Fe. The white dashed lines mark the boundary between the $L1_2$ Pt_3Fe shell and the random solid solution of $Pt_{65}Fe_{35}$. The red dashed circles mark the PtFe/Pt_3Fe boundary. (*G–J*) HAADF-STEM image and the corresponding STEM-EDS elemental mapping of the resultant PtFe/Pt core shell structure for a well-annealed $Pt_{65}Fe_{35}$ NP. (*K*) Schematic illustrating the interface mechanism of the ordering transformation.

weak intensity of Fe signal in the map, indicating the presence of a small amount of Fe in the Pt shell. Similar PtFe/Pt core–shell structure is confirmed by examining a large number of well-annealed $Pt_{65}Fe_{35}$ NPs, as shown in *SI Appendix*, Figs. S8 and S9.

The in situ STEM imaging in Fig. 3 shows that the ordering transformation in the $Pt_{65}Fe_{35}$ NPs starts from the rapid formation of an $L1_0$ PtFe skin that further transforms to $L1_2$ Pt_3Fe. The subsequent inward growth of the $L1_2$ Pt_3Fe shell toward the $Pt_{65}Fe_{35}$ solid solution core requires the supply of Pt atoms from the bulk in conjunction with the rejection of excess Fe atoms from the Pt_3Fe/$Pt_{65}Fe_{35}$ transformation boundary toward the core region. This counterdiffusion of Fe and Pt atoms in the course of the inward growth of the $L1_2$ Pt_3Fe shell results in the transfer of Pt atoms out of the core but Fe atoms into the core region. Therefore, the composition in the core region evolves to the stoichiometric ratio of intermetallic PtFe, greatly facilitating the nucleation of the $L1_0$ ordered PtFe in the core region. As shown in Fig. 3 *E* and *F*, the nucleated $L1_0$ ordered PtFe domain then grows outward by consuming the surrounding $L1_2$ ordered Pt_3Fe. The outward growth of the intermetallic PtFe core requires rejection of excess Pt atoms from the moving PtFe/Pt_3Fe boundary toward the surface region as well as the supply of Fe atoms from the Pt_3Fe in the surface region to reach the increased Pt/Fe stoichiometric ratio for PtFe, thereby inducing the sacrifice transformation of the Pt_3Fe in the surface region to a Pt shell. This outward growth of the PtFe core results in the Pt_3Fe decomposition into PtFe at the PtFe/

Pt_3Fe interface and into Pt in the surface region of the Pt_3Fe shell, which eventually leads to the formation of the PtFe/Pt core–shell structure consisting of the Pt shell and the $L1_0$ PtFe core, as confirmed by ex situ HAADF imaging and EDS mapping in Fig. 3 *G–J* and in situ HRTEM imaging (*SI Appendix*, Fig. S9).

Fig. 3*K* schematically illustrates the entire process of the ordering transformation in the $Pt_{65}Fe_{35}$ NPs. The ordering starts with the rapid formation of an $L1_0$ PtFe skin on the parent NP (Fig. 3 *K*, *i*). This is followed by the transformation of $L1_0$ PtFe skin to $L1_2$ Pt_3Fe and its inward growth via the outward diffusion of Pt atoms from the $Pt_{65}Fe_{35}$ core to the Pt_3Fe/$Pt_{65}Fe_{35}$ interface and inward diffusion of Fe atoms from the interface to the core (Fig. 3 *K*, *ii*). The counterdiffusion of Pt and Fe makes the composition in the core region evolve into the near-equal atomic ratio of Pt and Fe, thereby resulting in the nucleation of the $L1_0$ PtFe domain in the core region (Fig. 3 *K*, *iii*). The outward growth of the $L1_0$ PtFe core requires the outward rejection of Pt atoms from the PtFe/Pt_3Fe interface to the surface region and inward supply of Fe atoms from the surface region, thereby transforming the NP into a PtFe/Pt core–shell configuration by simultaneously decomposing the initially formed Pt_3Fe into PtFe in the core and into Pt in the surface region (Fig. 3 *K*, *iv*).

The in situ STEM imaging of the NPs shown above is performed under the vacuum annealing condition that results in the removal of the O-rich organic capping layer and oxygen on the NPs (more detail in *SI Appendix*, section SI-4), thereby rendering the intrinsic behavior of ordering transformations for
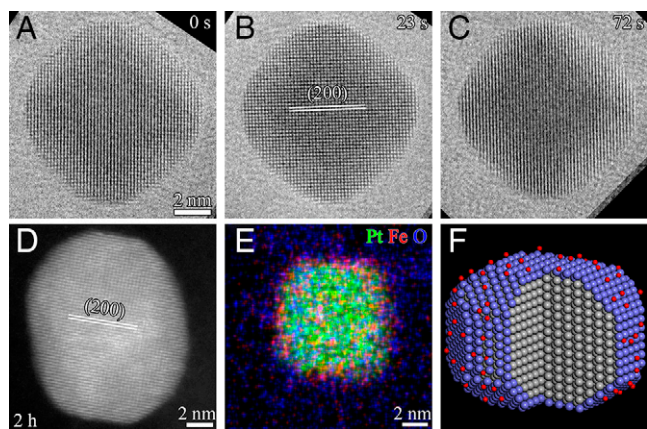
Fig. 4. In situ TEM imaging of $Pt_{85}Fe_{15}$ NPs during annealing at 700 °C in $pO_2 = 5 \times 10^{-3}$ Torr. (*A–C*) Sequence of in situ HRTEM images of a $Pt_{85}Fe_{15}$ NP during O_2 annealing. (*D*) HAADF-STEM image showing the random solid solution nature of a NP after 2-h O_2 annealing. (*E*) STEM-EDS mapping showing the presence of a FeO_x shell on a NP after 2-h O_2 annealing. (*F*) Schematic illustration of the core–shell structure of the NP consisting of a FeO_x shell and a Pt-rich random solid solution core. The gray, purple and red spheres represent the Pt-rich solid solution, Fe and O atoms, respectively.

clean NPs. We further examine the possible effect of ambient oxygen on ordering transformations in the NPs because of the ubiquitous presence of O_2 gas (more or less) in the annealing atmosphere for a practical heat-treatment process. Our in situ experiments are performed within the environment TEM that allows for temperature-, pressure-, and time-resolved observations of the structural transformation in the NPs by flowing O_2 gas in the sample area while simultaneously monitoring atomic structural evolution from the outermost surface layer to deeper atomic layers of the NP. Fig. 4 *A–C* show in situ HRTEM images of a $Pt_{85}Fe_{15}$ NP (viewed along the [001] zone axis) during the annealing at 700 °C in the O_2 flow of 5×10^{-3} Torr. The NP maintains the random solid solution without showing any noticeable ordering transformation throughout the annealing period (the slight loss of the two-dimensional lattice fringe image contrast in Fig. 4*C* is caused by thermally driven tilting of the NP at the elevated temperature, which results in the slight deviation from the [001] zone axis). This strong resistance to the ordering transformation in the NPs in the O_2 ambient is further confirmed by prolonged annealing. Fig. 4*D* illustrates a STEM-HAADF image of a $Pt_{85}Fe_{15}$ NP annealed at 700 °C in the O_2 flow of 5×10^{-3} Torr for 2 h, where the annealing time is more than twice of that shown in Fig. 2. The HAADF image shows the uniform image contrast of atom columns, indicating the random distribution of Pt and Fe atoms without undergoing chemical ordering (more examples given in *SI Appendix*, Fig. S10). Fig. 4*E* presents the STEM-EDS elemental mapping of a well-annealed NP in the O_2 ambient, in which the stronger intensity of Fe and O signal around the NP surface indicates that Fe is selectively oxidized as a FeO_x skin. Consistent with the EDS mapping, the corresponding electron energy-loss spectroscopy maps (see *SI Appendix*, Fig. S11) further confirm the selective oxidation of Fe from the O_2 annealing and resultant elemental redistribution. As a result, the O_2 annealing transforms the $Pt_{85}Fe_{15}$ NP into a core–shell structure consisting of an ultrathin FeO_x shell and a Pt-rich solid solution core. The selective oxidation of the minor element (Fe) results in the depletion of Fe in the alloy; therefore, the solid solution in the core becomes so dilute that it is effectively the pure component of Pt. Fig. 4*F* schematically

illustrates the Pt–FeO_x core–shell structure of the NP resulting from the O_2 annealing.

Fig. 5 *A–E* display time-sequence HRTEM images along the [001] zone axis, showing the structural evolution of a $Pt_{65}Fe_{35}$ NP during the annealing at 700 °C in $pO_2 = 5 \times 10^{-3}$ Torr. As marked by the dashed cyan circles in Fig. 5*B*, the superlattice domains become visible, signaling the onset of the ordering transformation via the nucleation and growth of $L1_2$ Pt_3Fe domains in the initially homogeneous solid solution NP. Meanwhile, an ultrathin, amorphous-like FeO_x skin develops around the NP surface (marked by the red dashed lines in Fig. 5*B*) due to the selective oxidation of Fe. Upon the continued O_2 annealing, the $L1_2$ Pt_3Fe domains expand and result in the formation of a $L1_2$ Pt_3Fe core. The selective oxidation of Fe is further evidenced by the expansion of the $L1_2$ Pt_3Fe domains and the thickening of the amorphous-like FeO_x shell around the NP, as marked by the dashed cyan and red circles, respectively, in Fig. 5*E*. As can be seen in Fig. 5*E*, an intermediate layer of the Pt-rich random solid solution exists between the inner $L1_2$ Pt_3Fe core and the outer FeO_x shell. The intermediate Pt-rich layer is formed due to the selective oxidation of Fe to form the FeO_x shell. Fig. 5*F* is a diffractogram of the HRTEM image in Fig. 5*E*, in which the sharp (100) and (110) superlattice reflections confirm the high degree of ordering in the $L1_2$ Pt_3Fe core. Fig. 5*G* presents a STEM-HAADF image of a well-annealed $Pt_{65}Fe_{35}$ NP (2 h at 700 °C in $pO_2 = 5 \times 10^{-3}$ Torr), showing the dominant formation of the $L1_2$ Pt_3Fe core along with the Pt-rich solid solution in the some of the subsurface region. The FeO_x formation at the outer surface is also visible in some region because of its large thickness, where the absence of crystalline lattice contrast in the HAADF image confirms the amorphous nature of the oxide. Fig. 5 *E* and *G* also show that the FeO_x clusters formed in the O_2 annealing tends to spread away from the $Pt_{65}Fe_{35}$ NPs (more examples in *SI Appendix*, Fig. S12), a behavior similar to the oxidation of $Pt_{0.5}Co_{0.5}$ NPs (34). Fig. 5*H* displays the corresponding STEM-EDS mapping, in which the strong intensity of O and Fe in the surface region corresponds to the FeO_x shell and the stronger intensity of Pt than that of Fe in the bulk region is related to the $L1_2$ Pt_3Fe intermetallic compound. The intermediate layer of the Pt-rich solid solution is not distinguishable in the EDS mapping due to its relatively low spatial resolution. More examples of the EDS mapping of the O_2 annealed $Pt_{65}Fe_{35}$ NPs are given in *SI Appendix*, Fig. S13, showing large Fe–O regions composed of Fe–O floccules and newly formed FeO_x clusters from the O_2 annealing. Fig. 5*I* schematically illustrates the resulting sandwich structure consisting of the $L1_2$ Pt_3Fe core, the intermediate layer of the Pt-rich solid solution, and the FeO_x shell from the O_2 annealing of $Pt_{65}Fe_{35}$ NPs.

Discussion

The as-synthesized Pt–Fe NPs are nearly square or rectangle shapes, dominated by {100} facets (Fig. 1). During the annealing process, the sharp corner regions evolve into the round shape driven by surface diffusion of atoms and have the tendency to further evolve into relatively flat {110} facets (i.e., round and truncated shapes), as shown in Figs. 2 and 3 and *SI Appendix*, Figs. S5–S9. Such annealing-induced shape changes to the NPs are consistent with other studies (3, 35, 36). More importantly, the in situ STEM imaging (Figs. 2 and 3) demonstrates the composition-dependent ordering transformations in Pt–Fe NPs. That is, the ordering transformation in $Pt_{85}Fe_{15}$
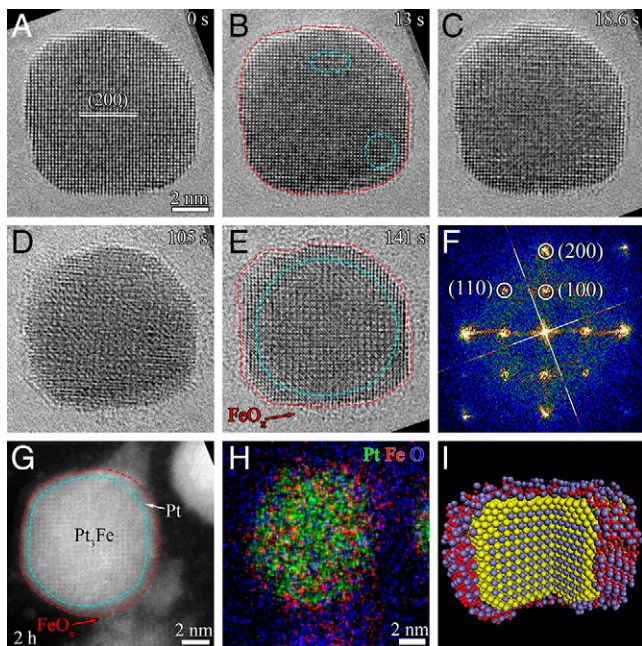
Fig. 5. In situ TEM imaging of $Pt_{65}Fe_{35}$ NPs during annealing at 700 °C in $pO_2 = 5 \times 10^{-3}$ Torr. (*A–E*) Time-sequence HRTEM images, showing that the selective oxidation of Fe along with the ordering transformation in the bulk of the NP during O_2 annealing results in a sandwich structure consisting of an amorphous-like FeO_x shell, a thin intermediate layer of Pt, and the $L1_2$ Pt_3Fe core. (*F*) Diffractogram of the HRTEM image in *E*, showing the (100) and (110) superlattice reflections associated with the $L1_2$ Pt_3Fe core. (*G*) HAADF-STEM image showing the presence of the $L1_2$ Pt_3Fe core in the NP annealed for 2 h at 700 °C in $pO_2 = 5 \times 10^{-3}$ Torr. The regions marked with the cyan dashed circles in *B*, *E*, and *G* correspond to the $L1_2$ Pt_3Fe structure. The red dashed circles mark the FeO_x/Pt boundary. (*H*) STEM-EDS mapping of an O_2-annealed NP, showing the presence of a FeO_x shell. (*I*) Schematic illustration of the FeO_x/Pt/Pt_3Fe sandwich structure of the NP from the O_2 annealing. The yellow, purple, and red spheres represent Pt, Fe, and O atoms, respectively.

NPs occurs via a nucleation and growth mechanism (Fig. 2*J*) but through an interface mechanism in $Pt_{65}Fe_{35}$ NPs (Fig. 3*K*). The nucleation and growth process of the ordering transformation in $Pt_{85}Fe_{15}$ NPs can be attributed to its large deviation of the alloy composition from the ideal stoichiometry of the intermetallic compounds of Pt–Fe. As shown from EDS line scan analysis in Fig. 1*D*, the surface region of the as-synthesized $Pt_{85}Fe_{15}$ NP is oxide-free with the significant enrichment of Pt over Fe. Therefore, the surface nucleation and growth of $L1_2$ Pt_3Fe domains results from both the long-range diffusion of Fe atoms from the bulk toward the surface and short-range diffusion of Fe and Pt atoms in the surface region for the nucleation of $L1_2$ Pt_3Fe domains.

By contrast, the ordering transformation in $Pt_{65}Fe_{35}$ NPs proceeds via the interface-controlled mechanism. As schematically illustrated in Fig. 3*K*, the entire surface of an NP is quickly transformed into a continuous thin skin of the $L1_0$ PtFe very soon after reaching 700 °C, where the $L1_0$ PtFe skin has a surface termination of Pt. This rapid formation of the $L1_0$ ordered PtFe skin can be attributed to the ready availability of Fe atoms in the surface region to participate in the PtFe formation around the NP surface. As shown in Fig. 1*H*, the as-synthesized $Pt_{65}Fe_{35}$ NPs exhibit Fe enrichment at the surface with an O-rich organic capping layer that can be removed by vacuum annealing (*SI Appendix*, Fig. S4) (37, 38). Therefore, Fe atoms are readily available in the surface region to alloy with nearby Pt atoms by short-range diffusion of Fe and Pt atoms without the need for a long-range supply of Fe from the

bulk. The Pt surface termination is driven by the lower surface energy of Pt than Fe ($\gamma_{Pt} \sim 2.79$ J/m², $\gamma_{Fe} \sim 3.55$ J/m²) (39–41). The surface segregation of Pt atoms from the bulk is accompanied by the inward migration of Fe atoms, which therefore subsequently transforms the $L1_0$ PtFe shell into the Pt-richer $L1_2$ Pt_3Fe.

The following inward advancement of the $L1_2$ Pt_3Fe involves the outward diffusion of Pt atoms from the core to the Pt_3Fe/$Pt_{65}Fe_{35}$ interface and inward diffusion of excess Fe atoms from the moving Pt_3Fe/$Pt_{65}Fe_{35}$ interface toward the core region. This counterdiffusion of Fe and Pt drives the alloy composition in the core region evolves to the stoichiometric ratio of intermetallic PtFe, greatly facilitating the nucleation of the $L1_0$ PtFe in the core region. The nucleated $L1_0$ PtFe domain grows outward by rejecting excess Pt atoms from the PtFe/Pt_3Fe interface toward the surface region and the inward supply of Fe atoms from the formed Pt_3Fe in the surface region, thereby resulting in the Pt surface shell by sacrificing the existing Pt_3Fe and eventually leading to the formation of the PtFe/Pt core–shell structure with the $L1_0$ PtFe core and the Pt shell, as shown in Fig. 3. For $Pt_{65}Fe_{35}$ NPs, this Pt_3Fe → PtFe transformation is driven by the strong Pt–Fe pairwise interactions and should be thermodynamically favorable because it leads to the maximized Pt–Fe bonds. By comparison, $Pt_{85}Fe_{15}$ NPs have a lower overall content of Fe and do not show the Pt_3Fe → PtFe transformation in the final configuration. This is because the $L1_2$ Pt_3Fe phase is thermodynamically more favorable than PtFe since the former allows for more abundant pairwise Pt–Fe atomic interactions for the relatively dilute Fe content in the $Pt_{85}Fe_{15}$ NPs.

To gain further understanding of the diffusion processes underlying the composition-dependent ordering transformations, we carried out density functional theory (DFT) calculations to predict the diffusion energetics in the two random Pt–Fe alloys. We used periodic supercells containing 108 atoms to model the Pt–Fe random alloys with the specific compositions of $Pt_{85}Fe_{15}$ and $Pt_{65}Fe_{35}$. In both cases, special quasirandom structures were generated using the ATAT code (42) to distribute Fe and Pt atoms randomly in an *fcc* lattice. Our DFT calculation predicts the equilibrium lattice parameters of an *fcc* unit cell to be 3.91 Å for $Pt_{85}Fe_{15}$ and 3.88 Å for $Pt_{65}Fe_{35}$, which are in good agreement with Vegard's law (29, 30). Moreover, we predict the vacancy formation energies and migration energies for vacancy-assisted diffusion in the Pt–Fe random alloys. The vacancy formation energies are calculated as the energy difference between the system containing a vacancy and the perfect crystal, taking into account the chemical potential change associated with the vacancy formation. In this work, the chemical potential of a Fe or Pt atom is adopted as the energy per atom in the pure body-centered cubic (*bcc*) Fe or *fcc* Pt crystal. It should be noted that the vacancies in the random alloys have different local chemical environments and hence different formation energies. Consequently, we calculate the formation energies for each type of the vacancies at four different chemical environments in terms of the varying local Fe concentration. The predicted vacancy formation energies are depicted in Fig. 6*A* for $Pt_{85}Fe_{15}$ and Fig. 6*C* for $Pt_{65}Fe_{35}$ alloys. We predict the average value of the formation energies to be 0.39 eV for a Fe vacancy and 1.26 eV for a Pt vacancy in $Pt_{85}Fe_{15}$ alloy, suggesting that Fe vacancies are favored to form in this alloy than Pt vacancies. In contrast, the average values of vacancy formation energies are found to be 1.84 eV for a Fe vacancy and 1.62 eV for a Pt vacancy in $Pt_{65}Fe_{35}$. It is worth mentioning that these predictions are close to the reported vacancy formation energies of 1.85 eV for a Fe vacancy and
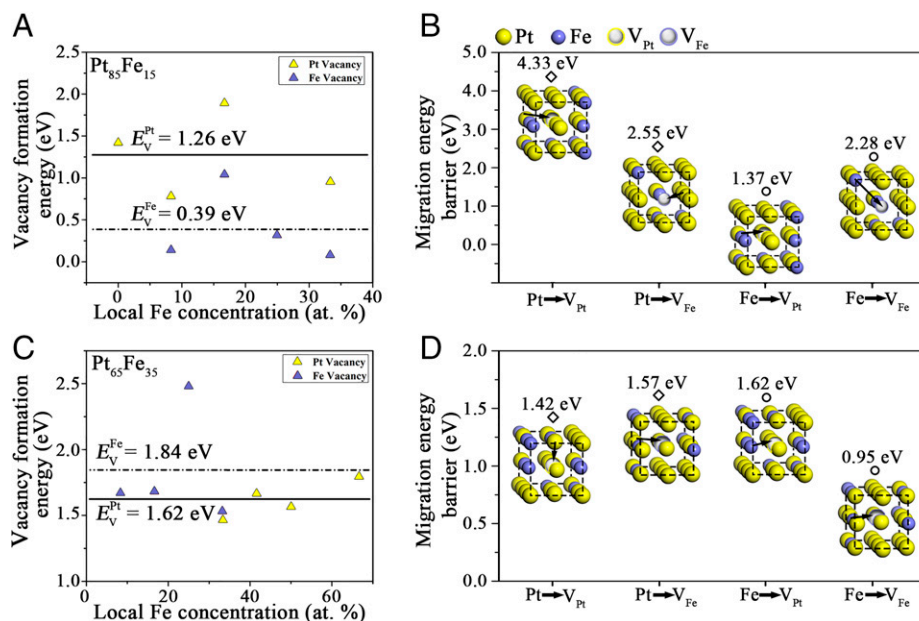
Fig. 6. DFT predicted vacancy formation energies and migration energies. (*A* and *B*) Vacancy formation energies in $Pt_{85}Fe_{15}$ and vacancy-assisted diffusion barriers in $Pt_{85}Fe_{15}$. (*C* and *D*) Vacancy formation energies and vacancy-assisted diffusion barriers in $Pt_{65}Fe_{35}$. The solid and dashed lines in *A* and *C* indicate the average vacancy formation energies of Pt and Fe, respectively. Local Fe concentration in *A* and *C* denotes the percentage of Fe among twelve nearest-neighboring atoms surrounding the vacancy. The paths of migration are presented with the black arrows from the migrating atoms to the vacancy.

1.70 eV for a Pt vacancy in $Fe_{50}Pt_{50}$ predicted using the coherent potential approximation (43, 44).

The observed Pt segregation at the NP surface is believed to be a result of a directional migration of the Fe or Pt atoms through the vacancy-exchange mechanism in the Pt–Fe NPs. Hence, we calculate the migration energies for the vacancy-assisted diffusion of Fe and Pt atoms in the two Pt–Fe alloys using the nudged elastic band (NEB) method (45). In this work, the migration path is defined as one atom moving to an adjacent vacancy. There are four types of diffusion paths, namely, a Pt atom to a Pt vacancy, an Fe atom to a Pt vacancy, a Pt atom to a Fe vacancy, and an Fe atom to a Fe vacancy, in the alloys. Our DFT results of the migration energy of Fe and Pt atoms are illustrated in Fig. 6*B* for $Pt_{85}Fe_{15}$ and Fig. 6*D* for $Pt_{65}Fe_{35}$ alloy. In $Pt_{85}Fe_{15}$ alloy, we predict that the migration energy of a Pt atom to an adjacent Pt vacancy could be as high as 4.36 eV, implying a very difficult movement of Pt atoms along this path. In addition, the predicted migration energy barrier of a Pt atom to a Fe vacancy (2.55 eV) is higher than those for a Fe atom to either a Pt vacancy (1.37 eV) or a Fe vacancy (2.28 eV). Consequently, our DFT results indicate that Fe is the faster-migrating species in $Pt_{85}Fe_{15}$. This corroborates well with our experimental observations showing that the ordering transformation in $Pt_{85}Fe_{15}$ NPs is initiated by the nucleation and growth of $L1_2$ Pt_3Fe domains at the surface, which requires the outward diffusion of Fe atoms from the bulk to the Pt-rich surface (Figs. 1*D* and 2 *A–D*). The later-stage ordering transformation in the core region of the NP requires the inward diffusion of Fe atoms from the surface region into the core (Fig. 2 *E* and *F*).

In $Pt_{65}Fe_{35}$, our DFT calculations show that the formation energy of a Pt vacancy is lower than that of a Fe vacancy. However, the migration energy of a Fe atom to an adjacent Fe vacancy is lower (0.95 eV) than the barriers for the migration of a Fe or Pt atom to a Pt vacancy (1.42 to 1.62 eV) (Fig. 6*D*). In the initial stage of the ordering transformation, the rapid formation of the $L1_0$ PtFe skin (Fig. 3*A*) can be related to the

small energy barrier for the inward migration of Fe atoms from the Fe-rich surface region. For the subsequent growth of Pt_3Fe and PtFe, the diffusion of Fe and Pt atoms can be equally important. This is because the smaller vacancy formation energy of Pt than that of Fe favors the generation of more Pt vacancies than Fe vacancies (thereby facilitating the diffusion of Pt and Fe atoms to Pt vacancies), whereas the lower energy barrier for the Fe migration of Fe vacancies promotes Fe diffusion. This is consistent with our in situ TEM observations, showing the inward advancement of the $L1_2$ Pt_3Fe shell by the counter-diffusion of Pt from the core to the $Pt_3Fe/Pt_{65}Fe_{35}$ interface and Fe from the moving $Pt_3Fe/Pt_{65}Fe_{35}$ interface toward the core region (Fig. 3 *B–D*) and the subsequent $Pt_3Fe \rightarrow PtFe$ transformation (Fig. 3 *E* and *F*) requiring the counterdiffusion of Pt from the $PtFe/Pt_3Fe$ interface to the surface region and Fe from the surface to the $PtFe/Pt_3Fe$ interface to result in the final $PtFe/Pt$ core–shell structure.

As discussed above, the ordering transformations are controlled by the vacancy-assisted diffusion of Pt and Fe atoms. Therefore, the availability of atomic vacancies in the alloys plays an important role in influencing the ordering kinetics. This effect is particularly clear by comparing the ordering transformation in $Pt_{65}Fe_{35}$ NPs for annealing in vacuum and O_2 ambient. As shown in Fig. 3 *A–D*, it takes ~60 min to fully transform the $Pt_{65}Fe_{35}$ NP into $L1_2$ Pt_3Fe for vacuum annealing at 700 °C. By contrast, the full transformation of the $Pt_{65}Fe_{35}$ NP into $L1_2$ Pt_3Fe takes only ~2 min for the O_2 annealing at 700 °C (Fig. 5 *A–E*). This significantly enhanced ordering kinetics in the O_2 ambient can be related to the selective oxidation of Fe to form FeO_x, which results in a large number of Fe vacancies in $Pt_{65}Fe_{35}$. As shown from our DFT calculations, the energy barrier for the migration of a Fe atom to a neighboring Fe vacancy is 0.95 eV, which is lower than all other diffusion paths (Fig. 6*D*) for $Pt_{65}Fe_{35}$. Therefore, the formation of a large number of Fe vacancies from the selective oxidation of Fe significantly promotes the diffusion of Fe in the

alloy, thereby dramatically accelerating ordering kinetics. By contrast, no ordering transformation is observed for the O_2 annealing of $Pt_{85}Fe_{15}$ NPs (Fig. 4). On one hand, the selective oxidation of Fe results in more Fe vacancies in the alloy and therefore enhances the mobility of atoms for potential ordering transformation. On the other hand, the selective oxidation of Fe also depletes Fe from the $Pt_{85}Fe_{15}$ alloy that is already Fe-poor, and therefore impairs the ordering because of the lack of sufficient Fe to form a Pt–Fe intermetallic compound.

In summary, we have used in situ TEM to directly monitor the ordering transformations in $Pt_{85}Fe_{15}$ and $Pt_{65}Fe_{35}$ NPs at the atomic scale. Our in situ atomic-scale observations demonstrate that the ordering in $Pt_{85}Fe_{15}$ NPs occurs via the surface nucleation and growth of $L1_2$ Pt_3Fe domains by long-range diffusion of Fe atoms from the bulk to the surface region. The ordering propagates inward with continued Pt_3Fe growth in the bulk and self-sacrifice transformation of the surface region of the formed $L1_2$ Pt_3Fe into a Pt skin, resulting in a core–shell structure consisting of the $L1_2$ Pt_3Fe core and the Pt shell. By contrast, the ordering in $Pt_{65}Fe_{35}$ NPs starts with the rapid formation of an $L1_0$ PtFe skin via short-range diffusion of Fe and Pt atoms in the surface region. The subsequent inward growth of the $L1_2$ Pt_3Fe shell results in the Fe enrichment in the core and thus drives the nucleation of $L1_0$ PtFe in the core. The outward growth of the $L1_0$ PtFe core is accompanied by the decomposition of the surface region of the formed $L1_2$ Pt_3Fe into a Pt skin, leading to a final core–shell structure consisting of the $L1_0$ PtFe core and a Pt shell. Our DFT calculations identify the composition-dependent vacancy-assisted counterdiffusion of Pt and Fe atoms between the surface and core regions in controlling the ordering transformation pathway. This vacancy-assisted diffusion is further demonstrated by annealing in O_2 ambient, for which the selective oxidation of Fe results in a large number of Fe vacancies in the alloy, thereby greatly accelerating the ordering kinetics that transforms the $Pt_{65}Fe_{35}$ NPs into a sandwich structure consisting of a FeO_x shell, an intermediate layer of Pt and an $L1_2$ Pt_3Fe core. By contrast, the O_2 annealing transforms $Pt_{85}Fe_{15}$ NPs into a core–shell structure composed of a FeO_x shell and Pt-rich solid solution core that is depleted with Fe for the selective oxidation of Fe in the alloy. These results provide unprecedented microscopic insights into the ordering transformation phenomena and their dependence on the alloy composition and chemical stimuli. Structurally ordered nanoalloys constitute an important subclass of metals and alloys and have attracted wide attention from the perspective of both fundamental understanding and potential applications, the results reported here are of wide relevance and considerable practical importance for a wide range of alloys, properties, and reactions, including metallurgy, nanostructure synthesis, corrosion, oxidation, and heterogeneous catalysis.

Materials and Methods

Synthesis of Random Solid Solutions of Pt–Fe NPs. Pt–Fe NPs were prepared using a modified method reported previously (28) and more detail is given in *SI Appendix*, sections SI 1–3. Composition analysis of the as-synthesized NPs was performed using an Optima 7000 DV ICP-OES (inductively coupled plasma optical emission spectrometry) spectrometer, EDS, and synchrotron X-ray diffraction measurements on the lattice spacings. In addition to the EDS linescan analysis performed on individual NPs (Fig. 1 *D* and *H*), EDS mapping of a collection of as-synthesized NPs (*SI Appendix*, Fig. S3) further confirms the more Fe enrichment in the surface region of $Pt_{65}Fe_{35}$ NPs than that in $Pt_{85}Fe_{15}$ NPs. The EDS mapping also shows that the as-synthesized $Pt_{85}Fe_{15}$ and $Pt_{65}Fe_{35}$ NPs are covered with an O-rich organic capping layer. This capping layer can be largely removed by vacuum annealing (*SI Appendix*, Fig. S4), consistent with other

studies (37, 38). The as-synthesized $Pt_{65}Fe_{35}$ NPs have a small amount of Fe-O floccules, as confirmed by XRD (*SI Appendix*, Fig. S2), HAADF and EDS mapping (*SI Appendix*, Fig. S4), and ICP-OES (*SI Appendix*, Table S1). These Fe–O floccules remain stable without decomposition under the vacuum annealing (*SI Appendix*, Fig. S4). By contrast, the as-synthesized $Pt_{85}Fe_{15}$ NPs are free of Fe–O floccules.

In Situ STEM and TEM Characterization. The as-prepared Pt–Fe NPs were loaded on SiN_x thin film of DENSsolution chips showing homogeneity and monodispersity. Real-time HAADF-STEM observations of the ordering transformation in the NPs were performed using a MEMS-based heating holder (DENSsolution) with FEI Talos F200X microscopy operated at 200 kV and equipped with a four-quadrant EDS detector for elemental mapping and line scan analysis. STEM EDS mapping was performed after rapidly cooling (quenching) the NPs from 700 °C to room temperature. The "dot-like" intensity feature in the EDS maps is related to the poor counting statistics, not representative of the real chemical composition. In situ HRTEM observations of the ordering transformation in the oxygen gas ambient were performed using a dedicated environmental TEM (FEI Titan 80-300) equipped with an objective-lens aberration corrector and a differential pumping system that allows flowing O_2 gas (purity 99.9999%) with $pO_2 = 5 \times 10^{-3}$ Torr in the sample area. The spatial resolution of this environmental microscopy is about 0.8 Å, even at the elevated gas pressure and temperature local to the specimen areas. The heating holder allows specimen annealing at 700 °C at a heating rate of 100 °C/min from room temperature along with ~1 min for the sample stabilization from the thermal drift at 700 °C before STEM and TEM observations.

DFT Calculations. The DFT calculations were performed using the Vienna ab initio simulation package (VASP) (46). The projector augmented wave pseudopotential (47) was used to describe the core electrons of the elements. The energy cutoff was set as 500 eV to expand wave function. The generalized gradient approximation with the Perdew–Burke–Ernzerhof (48) exchange-correlation functional was used to evaluate the exchange-correlation energy. In all calculations, the total energy of system was converged within 10^{-6} eV. A Monkhorst-Pack k-point grid of $4 \times 4 \times 4$ was used in these calculations. All the structures were fully relaxed until the force acting on each atom was lower than 0.01 eV/Å. The transition states of vacancy migration were located using the NEB method (46), in which the forces along and perpendicular to the path were relaxed to less than 0.05 eV/Å. In each NEB calculation, we used three intermediate images to locate the transition state and calculated the migration energy as the energy difference between the transition state and the initial state.

Data Availability. All study data are included in the article and/or *SI Appendix*.

Author affiliations: ªMaterials Science and Engineering Program, State University of New York at Binghamton, Binghamton, NY 13902; ᵇDepartment of Mechanical Engineering, State University of New York at Binghamton, Binghamton, NY 13902; ᶜDepartment of Mechanical Engineering and Materials Science, University of Pittsburgh, Pittsburgh, PA 15261; ᵈDepartment of Chemistry, State University of New York at Binghamton, Binghamton, NY 13902; ᵉCenter for Functional Nanomaterials, Brookhaven National Laboratory, Upton, NY 11973; ᶠDepartment of Condensed Matter Physics and Materials, Brookhaven National Laboratory, Upton, NY 11973; and ᵍSchool of Physics and Microelectronics, Zhengzhou University, Zhengzhou 450052, China

1. D. A. Porter, K. E. Easterling, M. Y. Sherif, *Phase Transformations in Metals and Alloys* (CRC Press, ed. 3, 2009), pp. 11–26.
2. S. Müller, Bulk and surface ordering phenomena in binary metal alloys. *J. Phys. Condens. Matter* **15**, 1429–1500 (2003).
3. M. Chi *et al.*, Surface faceting and elemental diffusion behaviour at atomic scale for alloy nanoparticles during in situ annealing. *Nat. Commun.* **6**, 8925 (2015).
4. F. Li *et al.*, Atomistic imaging of competition between surface diffusion and phase transition during the intermetallic formation of faceted particles. *ACS Nano* **15**, 5284–5293 (2021).
5. Y. Xiong *et al.*, Revealing the atomic ordering of binary intermetallics using in situ heating techniques at multilength scales. *Proc. Natl. Acad. Sci. U.S.A.* **116**, 1974–1983 (2019).
6. S. Dai *et al.*, In situ atomic-scale observation of oxygen-driven core-shell formation in Pt_3Co nanoparticles. *Nat. Commun.* **8**, 204 (2017).
7. T. Avanesian *et al.*, Quantitative and atomic-scale view of CO-induced Pt nanoparticle surface reconstruction at saturation coverage via DFT calculations coupled with in situ TEM and IR. *J. Am. Chem. Soc.* **139**, 4551–4558 (2017).
8. D. Alloyeau *et al.*, Size and shape effects on the order-disorder phase transition in CoPt nanoparticles. *Nat. Mater.* **8**, 940–946 (2009).
9. J. Li, S. Sun, Intermetallic nanoparticles: Synthetic control and their enhanced electrocatalysis. *Acc. Chem. Res.* **52**, 2015–2025 (2019).
10. M. Zhou, C. Li, J. Fang, Noble-metal based random alloy and intermetallic nanocrystals: Syntheses and applications. *Chem. Rev.* **121**, 736–795 (2021).
11. W. Xiao, W. Lei, M. Gong, H. L. Xin, D. Wang, Recent advances of structurally ordered intermetallic nanoparticles for electrocatalysis. *ACS Catal.* **8**, 3237–3256 (2018).
12. V. R. Stamenkovic *et al.*, Trends in electrocatalysis on extended and nanoscale Pt-bimetallic alloy surfaces. *Nat. Mater.* **6**, 241–247 (2007).
13. L. Bu *et al.*, A general method for multimetallic platinum alloy nanowires as highly active and stable oxygen reduction catalysts. *Adv. Mater.* **27**, 7204–7212 (2015).
14. M. Liu, Z. Zhao, X. Duan, Y. Huang, Nanoscale structure design for high-performance Pt-based ORR catalysts. *Adv. Mater.* **31**, e1802234 (2019).
15. M. Shao, Q. Chang, J. P. Dodelet, R. Chenitz, Recent advances in electrocatalysts for oxygen reduction reaction. *Chem. Rev.* **116**, 3594–3657 (2016).
16. Q. Shi, C. Zhu, D. Du, Y. Lin, Robust noble metal-based electrocatalysts for oxygen evolution reaction. *Chem. Soc. Rev.* **48**, 3181–3192 (2019).
17. J. T. L. Gamler, H. M. Ashberry, S. E. Skrabalak, K. M. Koczkur, Random alloyed versus intermetallic nanoparticles: A comparison of electrocatalytic performance. *Adv. Mater.* **30**, e1801563 (2018).
18. Y. Yan *et al.*, Intermetallic nanocrystals: Syntheses and catalytic applications. *Adv. Mater.* **29**, 1605997 (2017).
19. G. Jiang *et al.*, Core/shell face-centered tetragonal FePd/Pd nanoparticles as an efficient non-Pt catalyst for the oxygen reduction reaction. *ACS Nano* **9**, 11014–11022 (2015).
20. J. Greeley *et al.*, Alloys of platinum and early transition metals as oxygen reduction electrocatalysts. *Nat. Chem.* **1**, 552–556 (2009).
21. L. Bu *et al.*, Coupled s-p-d exchange in facet-controlled Pd_3Pb tripods enhances oxygen reduction catalysis. *Chem* **4**, 359–371 (2018).
22. L. Rößner, M. Armbrüster, Electrochemical energy conversion on intermetallic compounds: A review. *ACS Catal.* **9**, 2018–2062 (2019).
23. D. Kim *et al.*, Electrochemical activation of CO_2 through atomic ordering transformations of AuCu nanoparticles. *J. Am. Chem. Soc.* **139**, 8329–8336 (2017).
24. Y. Yu *et al.*, A facile solution phase synthesis of directly ordering monodisperse FePt nanoparticles. *Nano Res.* **15**, 446–451 (2022).
25. M. C. Saint-Lager *et al.*, Oxygen-induced changes of the $Au_{30}Pd_{70}(110)$ surface structure and composition under increasing O_2 pressure. *J. Phys. Chem. C* **122**, 22588–22596 (2018).
26. S. Nakanishi *et al.*, Oxygen induced surface segregation of Cu on the $Au_{0.7}Cu_{0.3}$ (100) surface. *Surf. Sci. Lett.* **247**, L215–L220 (1991).
27. S. Prabhudev, M. Bugnet, G.-Z. Zhu, C. Bock, G. A. Botton, Surface segregation of Fe in Pt–Fe alloy nanoparticles: Its precedence and effect on the ordered-phase evolution during thermal annealing. *ChemCatChem* **7**, 3655–3664 (2015).
28. J. Zhang, J. Fang, A general strategy for preparation of Pt 3d-transition metal (Co, Fe, Ni) nanocubes. *J. Am. Chem. Soc.* **131**, 18543–18547 (2009).
29. K. Kusada *et al.*, Solid solution alloy nanoparticles of immiscible Pd and Ru elements neighboring on Rh: Changeover of the thermodynamic behavior for hydrogen storage and enhanced CO-oxidizing ability. *J. Am. Chem. Soc.* **136**, 1864–1871 (2014).
30. F. Wang *et al.*, Solid-solution alloy nanoparticles of the immiscible iridium-copper system with a wide composition range for enhanced electrocatalytic applications. *Angew. Chem. Int. Ed. Engl.* **57**, 4505–4509 (2018).
31. A. V. Ruban, Surface composition of ordered alloys: An off-stoichiometric effect. *Phys. Rev. B Condens. Matter Mater. Phys.* **65**, 174201 (2002).
32. M. Polak, L. Rubinovich, The interplay of surface segregation and atomic order in alloys. *Surf. Sci. Rep.* **38**, 127–194 (2000).
33. C. Creemers, P. Deurinck, Platinum segregation to the (111) surface of ordered $Pt_{80}Fe_{20}$: LEIS results and model simulations. *Surf. Interface Anal.* **25**, 177–190 (1997).
34. H. L. Xin *et al.*, Revealing the atomic restructuring of Pt-Co nanoparticles. *Nano Lett.* **14**, 3203–3207 (2014).
35. P. L. Hansen *et al.*, Atom-resolved imaging of dynamic shape changes in supported copper nanocrystals. *Science* **295**, 2053–2055 (2002).
36. X. Zhang *et al.*, In situ TEM studies of the shape evolution of Pd nanocrystals under oxygen and hydrogen environments at atmospheric pressure. *Chem. Commun. (Camb.)* **53**, 13213–13216 (2017).
37. T. H. Yang, Y. Shi, A. Janssen, Y. Xia, Surface capping agents and their roles in shape-controlled synthesis of colloidal metal nanocrystals. *Angew. Chem. Int. Ed. Engl.* **59**, 15378–15401 (2020).
38. D. Li *et al.*, Surfactant removal for colloidal nanoparticles from solution synthesis: The effect on catalytic performance. *ACS Catal.* **2**, 1358–1362 (2012).
39. A. Patra, S. Jana, L. A. Constantin, L. Chiodo, P. Samal, Improved transition metal surface energies from a generalized gradient approximation developed for quasi two-dimensional systems. *J. Chem. Phys.* **152**, 151101 (2020).
40. A. V. Ruban, H. L. Skriver, J. K. Nørskov, Surface segregation energies in transition-metal alloys. *Phys. Rev. B Condens. Matter Mater. Phys.* **59**, 15990–16000 (1999).
41. A. U. Nilekar, A. V. Ruban, M. Mavrikakis, Surface segregation energies in low-index open surfaces of bimetallic transition metal alloys. *Surf. Sci.* **603**, 91–96 (2009).
42. A. Van De Walle *et al.*, Efficient stochastic generation of special quasirandom structures. *Calphad* **42**, 13–18 (2013).
43. M. Müller, K. Albe, Kinetic lattice Monte-Carlo simulations on the ordering kinetics of free and supported FePt L1(0)-nanoparticles. *Beilstein J. Nanotechnol.* **2**, 40–46 (2011).
44. A. Alam, B. Kraczek, D. D. Johnson, Structural, magnetic, and defect properties of Co-Pt-type magnetic-storage alloys: Density-functional theory study of thermal processing effects. *Phys. Rev. B Condens. Matter Mater. Phys.* **82**, 024435 (2010).
45. G. Henkelman, B. P. Uberuaga, H. Jónsson, Climbing image nudged elastic band method for finding saddle points and minimum energy paths. *J. Chem. Phys.* **113**, 9901–9904 (2000).
46. G. Kresse, J. Furthmüller, Efficient iterative schemes for ab initio total-energy calculations using a plane-wave basis set. *Phys. Rev. B Condens. Matter* **54**, 11169–11186 (1996).
47. G. Kresse, D. Joubert, From ultrasoft pseudopotentials to the projector augmented-wave method. *Phys. Rev. B Condens. Matter Mater. Phys.* **59**, 1758 (1999).
48. J. P. Perdew, K. Burke, M. Ernzerhof, Generalized gradient approximation made simple. *Phys. Rev. Lett.* **77**, 3865–3868 (1996).